

field are seen in the THEMIS data (Fig. 2), yet are absent or barely discernible in the MOC wide-angle camera (MOC WA) and Mars Orbiter Laser Altimeter topographic data. One MOC NA image crosses several of these features and reveals that they are exposures of underlying bright terrain where dunes are not present (Fig. 4c). These features are probably locations of aeolian scour, which has exposed unit E from beneath the pervasive dune field.

The ubiquitous exposure of unit E within unit Ph strongly suggests that it underlies all of the haematite-rich plains. Unit E is exposed in craters of all sizes, down to the resolution of the MOC NA images (~2 m), indicating that unit Ph is very thin. In all cases, unit E appears as bright, high thermal inertia outcrops that contrast sharply with unit Ph. Evidence of expansive dune fields and embayment of positive topographic expressions of unit E suggests that the thin, dark, haematite-bearing layer is mobile and may be the primary soil constituent. Unit Ph is probably a lag deposit made of dense, coarse, haematite-rich grains derived from the erosion of previously existing overlying layers, and this is the source of the haematite signature detected by the TES instrument. Conversely, unit E consists of in-place underlying bedrock, as is evident from its high thermal inertia and its layered exposures seen in images.

In the Opportunity landing site crater, ~1/2-m-thick, finely layered units are exposed in the rim³ and embayed by dark, haematite-rich soil¹⁵. These outcrops are probably the uppermost expressions of unit E and correlate with light-toned layers observed throughout the haematite-bearing plain, an area of 1×10^5 km². Moreover, unit E outcrops along roughly half of the unit Ph margin and is mappable over hundreds of kilometres to the east, north and west. In places, unit E disappears underneath younger mantling materials, masking its full extent. In totality, exposures of this etched material cover an area of 3.3×10^5 km² that spans 20° of longitude and 14° of latitude, more than three times the extent of the haematite-bearing plain itself. Opportunity has detected high concentrations of sulphur-bearing minerals and unique textures in the observed bedrock that are indicative of water saturation for long periods of time³. Thus, whatever aqueous process altered, and perhaps formed, the layered units at the landing site³ must have acted over an extensive area and a large volume of material. If the outcrops at the landing site are indeed a result of deposition in a sea, then that body of water had to be comparable in area to Earth's Baltic Sea and must have been deep enough, and persisted long enough, to build up at least a 0.5-km-thick stack of sediments. For this to occur, the ancient global climate of Mars must have been very different from its present climate and have lasted for an extended period. □

Received 20 April; accepted 28 July 2004; doi:10.1038/nature02902.

1. Christensen, P. R. *et al.* Detection of crystalline hematite mineralization on Mars by the Thermal Emission Spectrometer: Evidence for near-surface water. *J. Geophys. Res.* **105**, 9623–9642 (2000).
2. Christensen, P. R., Morris, R. V., Lane, M. D., Bandfield, J. L. & Malin, M. C. Global mapping of martian hematite mineral deposits: Remnants of water-driven processes on early Mars. *J. Geophys. Res.* **106**, 23873–23886 (2001).
3. Squyres, S. W. *et al.* Initial results from the MER ATHENA science investigation at Gusev Crater and Meridiani Planum. *Lunar Planet. Sci. Conf. XXXV*, 2187 (2004).
4. Hynek, B. M., Arvidson, R. E. & Phillips, R. J. Geologic setting and origin of Terra Meridiani hematite deposit on Mars. *J. Geophys. Res.* **107**, doi:10.1029/2002JE001891 (2002).
5. Lane, M. D., Christensen, P. R. & Hartmann, W. K. Utilization of the THEMIS visible and infrared imaging data for crater population studies of the Meridiani Planum landing site. *Geophys. Res. Lett.* **30**, doi:10.1029/2003GL017183 (2003).
6. Edgett, K. S. & Malin, M. C. Martian sedimentary rock stratigraphy: Outcrops and interbedded craters of northwest Sinus Meridiani and southwest Arabia Terra. *Geophys. Res. Lett.* **29**, doi:10.1029/2002GL016515 (2002).
7. Arvidson, R. E. *et al.* Mantled and exhumed terrains in Terra Meridiani, Mars. *J. Geophys. Res.* **108**, doi:10.1029/2002JE001982 (2003).
8. Palluconi, F. D. & Kieffer, H. H. Thermal inertia mapping of Mars from 60 degrees S to 60 degrees N. *Icarus* **45**, 415–426 (1981).
9. Mellon, M. T., Jakosky, B. M., Kieffer, H. H. & Christensen, P. R. High-resolution thermal inertia mapping from the Mars Global Surveyor Thermal Emission Spectrometer. *Icarus* **148**, 437–455 (2000).
10. Tanaka, K. L. Dust and ice deposition in the martian geologic record. *Icarus* **144**, 254–266 (2000).
11. Malin, M. C. & Edgett, K. S. Sedimentary rocks of early Mars. *Science* **290**, 1927–1937 (2000).
12. Malin, M. C. & Edgett, K. S. Mars Global Surveyor Mars Orbiter Camera: Interplanetary cruise through primary mission. *J. Geophys. Res.* **106**, 23429–23570 (2001).

13. Hynek, B. M., Phillips, R. J. & Arvidson, R. E. Explosive volcanism in the Tharsis region: Global evidence in the martian geologic record. *J. Geophys. Res.* **108**, doi:10.1029/2003JE002062 (2003).
14. Hynek, B. M. *et al.* Thermophysical properties of Meridiani Planum, Mars. *Lunar Planet. Sci. Conf. XXXV*, 1899 (2004).
15. Christensen, P. R. *et al.* Mini-TES observations of the Gusev and Meridiani landing sites. *Lunar Planet. Sci. Conf. XXXV*, 2186 (2004).
16. Putzig, N. E. *et al.* Mars thermal inertia from THEMIS data. *Lunar Planet. Sci. Conf. XXXV*, 1863 (2004).
17. Jakosky, B. M. *et al.* Remote-sensing of the thermophysical properties of the MER and Beagle II landing sites on Mars. *J. Geophys. Res.* (submitted) (2004).

Acknowledgements I thank N. E. Putzig and M. T. Mellon for THEMIS-derived thermal inertia products used in this study and B. M. Jakosky and J. R. Zimbleman for comments on this manuscript. This work was supported by the National Aeronautics and Space Agency (NASA).

Competing interests statement The authors declare that they have no competing financial interests.

Correspondence and requests for materials should be addressed to B.M.H. (brian.hynek@lasp.colorado.edu).

Coherent dynamics of a flux qubit coupled to a harmonic oscillator

I. Chiorescu^{1*}, P. Bertet¹, K. Semba^{1,2}, Y. Nakamura^{1,3}, C. J. P. M. Harmans¹ & J. E. Mooij¹

¹Quantum Transport group, Kavli Institute of NanoScience, Delft University of Technology and Delft Institute for Micro Electronics and Submicron Technology (DIMES), Lorentzweg 1, 2628 CJ, Delft, The Netherlands

²NTT Basic Research Laboratories, NTT Corporation, 3-1 Morinosato-Wakamiya, Atsugi 243-0198, Japan

³NEC Fundamental Research Laboratories, 34 Miyukigaoka, Tsukuba, Ibaraki 305-8501, Japan

* Present address: Department of Physics and Astronomy, Michigan State University, East Lansing, Michigan 48824, USA

In the emerging field of quantum computation¹ and quantum information, superconducting devices are promising candidates for the implementation of solid-state quantum bits (qubits). Single-qubit operations^{2–6}, direct coupling between two qubits^{7–10} and the realization of a quantum gate¹¹ have been reported. However, complex manipulation of entangled states—such as the coupling of a two-level system to a quantum harmonic oscillator, as demonstrated in ion/atom-trap experiments^{12,13} and cavity quantum electrodynamics¹⁴—has yet to be achieved for superconducting devices. Here we demonstrate entanglement between a superconducting flux qubit (a two-level system) and a superconducting quantum interference device (SQUID). The latter provides the measurement system for detecting the quantum states; it is also an effective inductance that, in parallel with an external shunt capacitance, acts as a harmonic oscillator. We achieve generation and control of the entangled state by performing microwave spectroscopy and detecting the resultant Rabi oscillations of the coupled system.

The device was realized by electron-beam lithography and metal evaporation. The qubit–SQUID geometry is shown in Fig. 1a: a large loop interrupted by two Josephson junctions (the SQUID) is merged with the smaller loop on the right-hand side comprising three in-line Josephson junctions (the flux qubit)¹⁵. By applying a perpendicular external magnetic field, the qubit is biased around $\Phi_0/2$, where $\Phi_0 = h/2e$ is the flux quantum. Previous spectroscopy¹⁶ and coherent time-domain experiments⁶ have shown that the flux qubit is a controllable two-level system with ‘spin-up/spin-down’ states corresponding to persistent currents flowing in ‘clockwise/

anticlockwise' directions and coupled by tunnelling. Here we show that a stronger qubit-SQUID coupling allows us to investigate the coupled dynamics of a 'qubit-harmonic oscillator' system.

The qubit hamiltonian is defined by the charging and Josephson energy of the qubit outer junctions ($E_C = e^2/2C$ and $E_J = \hbar I_C/4\pi e$, where C and I_C are their capacitance and critical current)¹⁶. In a

two-level truncation, the hamiltonian becomes $H_q/\hbar = -\varepsilon\sigma_z/2 - \Delta\sigma_x/2$, where $\sigma_{z,x}$ are the Pauli matrices in the spin-up/spin-down basis, Δ is the tunnel splitting and $\varepsilon \approx I_p\Phi_0(\gamma_q - \pi)/\hbar\pi$ (I_p is the qubit maximum persistent current and γ_q is the superconductor phase across the three junctions). The resulting energy level spacing represents the qubit Larmor frequency $F_L = \sqrt{\Delta^2 + \varepsilon^2}$. The SQUID dynamics is characterized by the Josephson inductance of the junctions $L_J \approx 80$ pH, shunt capacitance $C_{sh} \approx 12$ pF (see Fig. 1a) and self-inductances $L_{sl} \approx 170$ pH of the SQUID and shunt-lines. In our experiments, the SQUID circuit behaves like a harmonic oscillator described by $H_{sq} = \hbar\nu_p(a^\dagger a + 1/2)$, where $2\pi\nu_p = 1/\sqrt{(L_J + L_{sl})C_{sh}}$ is called the plasma frequency and a (a^\dagger) is the plasmon annihilation (creation) operator. Henceforth $|\beta n\rangle$ represents the state with the qubit in the ground ($\beta = 0$) or excited ($\beta = 1$) level, and the oscillator on the n th level ($n = 0, 1, 2, \dots$). The corresponding level diagram is sketched in Fig. 1b (inset). The coupling between the qubit and the oscillator originates from the current distribution in the shared branches (Fig. 1a), and gives rise to an interaction hamiltonian $H_{q-sq} = \lambda\sigma_z(a + a^\dagger)$ with $\lambda \approx 0.2$ GHz in our device¹⁷ (the estimated qubit-SQUID coupling is $M \approx 20$ pH).

Measurements are performed at $T = 25$ mK using low-noise circuitry to minimize decoherence, relaxation and thermal activation. The system is first initialized by allowing it to relax to the $|00\rangle$ ground state. With successive resonant microwave pulses we achieve controlled superposition of various $|\beta n\rangle$ states, as shown below. The readout⁶ is performed by applying a short current pulse I_b (~ 30 ns) and by monitoring whether the SQUID switches to the finite-voltage state. After averaging typically 10,000 readouts, we obtain the probability $P_{sw}(I_b)$ which for properly chosen parameters is proportional to the excited state occupancy. In the

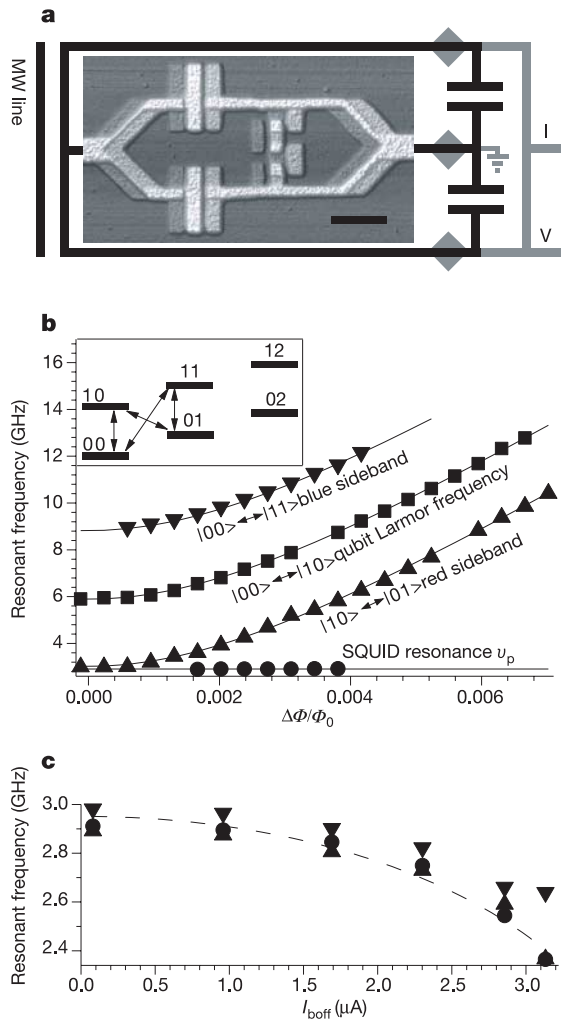


Figure 1 Qubit-SQUID device and spectroscopy. **a**, Atomic force micrograph of the SQUID (large loop) merged with the flux qubit (the smallest loop closed by three junctions); the qubit to SQUID area ratio is 0.37. Scale bar, 1 μ m. The SQUID (qubit) junctions have a critical current of 4.2 (0.45) μ A. The device is made of aluminium by two symmetrically angled evaporations with an oxidation step in between. The surrounding circuit shows aluminium shunt capacitors and lines (in black) and gold quasiparticle traps³ and resistive leads (in grey). The microwave field is provided by the shortcut of a coplanar waveguide (MW line) and couples inductively to the qubit. The current line (I) delivers the readout pulses, and the switching event is detected on the voltage line (V). **b**, Resonant frequencies indicated by peaks in the SQUID switching probability when a long microwave pulse excites the system before the readout pulse. Data are represented as a function of the external flux through the qubit area away from the qubit symmetry point. Inset, energy levels of the qubit-oscillator system for some given bias point. The blue and red sidebands are shown by down- and up-triangles, respectively; continuous lines are obtained by adding 2.96 GHz and -2.90 GHz, respectively, to the central continuous line (numerical fit). These values are close to the oscillator resonance ν_p at 2.91 GHz (solid circles), and we attribute the small differences to the slight dependence of ν_p on qubit state. **c**, The plasma resonance (circles) and the distances between the qubit peak (here $F_L = 6.4$ GHz) and the red/blue (up/down triangles) sidebands as a function of an offset current I_{boff} through the SQUID. The data are close to each other and agree well with the theoretical prediction for ν_p versus offset current (dashed line).

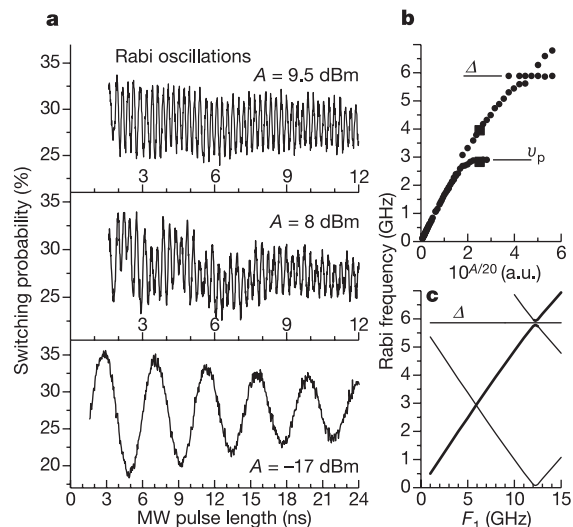


Figure 2 Rabi oscillations at the qubit symmetry point $\Delta = 5.9$ GHz. **a**, Switching probability as a function of the microwave pulse length for three microwave nominal powers; decay times are of the order of 25 ns. For $A = 8$ dBm, bi-modal beatings are visible (the corresponding frequencies are shown by the filled squares in **b**). **b**, Rabi frequency, obtained by fast Fourier transformation of the corresponding oscillations, versus microwave amplitude. In the weak driving regime, the linear dependence is in agreement with estimations based on sample design. A first splitting appears when the Rabi frequency is $\sim \nu_p$. In the strong driving regime, the power independent Larmor precession at frequency Δ gives rise to a second splitting. **c**, This last aspect is obtained in numerical simulations where the microwave driving is represented by a term $(1/2)\hbar F_1 \cos(\Delta t)$ and a small deviation from the symmetry point (100 MHz) is introduced in the strong driving regime (the thick line indicates the main Fourier peaks). Radiative shifts²⁰ at high microwave power could account for such a shift in the experiment.

following, we first show the spectroscopy of the coupled qubit–oscillator system and Rabi oscillations of the qubit. Next we demonstrate coherent dynamics of the coupled system.

We performed spectroscopy of the coupled qubit–oscillator system by applying a long (300 ns) microwave pulse with various frequencies and measuring the SQUID switching probability. Peaks and dips are observed and their resonant frequencies as a function of $\Delta\Phi = \Phi_{\text{ext}} - \Phi_0/2$ are given in Fig. 1b. We obtain one manifold of three resonances spaced by ~ 2.91 GHz. This frequency coincides with the designed oscillator eigenfrequency ν_p . In addition, we observe a spectroscopic peak or dip that depends only weakly on the magnetic field (circles in Fig. 1b). For lower microwave power, only the qubit band (squares) remains visible. A numerical fit (continuous line) of this band leads to $E_J = 225$ GHz, $E_C = 7.3$ GHz, and the ratio of area of qubit junctions $\alpha = 0.76$ ($\Delta = 5.9$ GHz, $I_p = 275$ nA). The appearance of the manifold instead of a single resonance is due to the qubit coupling with the oscillator mode ν_p (ref. 18). Similarly to atomic physics, we call the $|00\rangle$ to $|11\rangle$ ($|01\rangle$ to $|10\rangle$) transitions the blue (red) sidebands (see the ladder energy diagram of the $|\beta n\rangle$ states in Fig. 1b inset). We note that near the qubit symmetry point, the closeness of the oscillator resonance and the red sideband, visible owing to a small thermal occupation of the $|01\rangle$ state, is purely accidental. To verify that

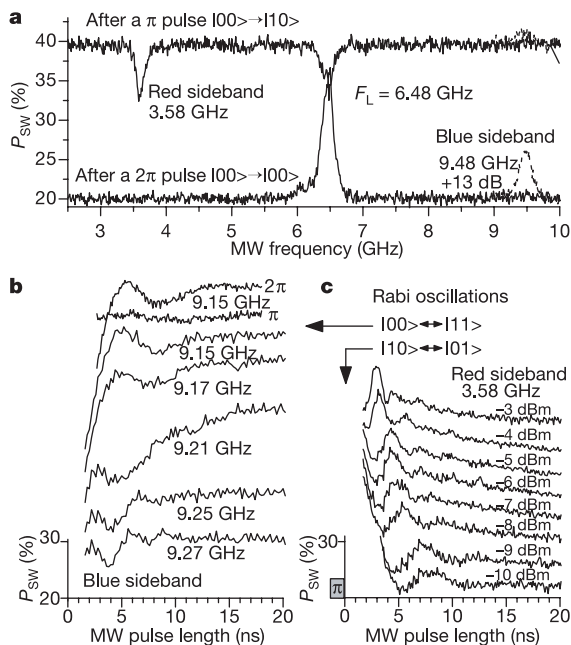


Figure 3 Generation and control of entangled states. **a**, Spectroscopic characterization of the energy levels (see Fig. 1b inset) after a π (upper scan) and a 2π (lower scan) Rabi pulse on the qubit transition. In the upper scan, the system is first excited to $|10\rangle$, from which it decays towards the $|01\rangle$ excited state (red sideband at 3.58 GHz) or towards the $|00\rangle$ ground state ($F_L = 6.48$ GHz). In the lower scan, the system is rotated back to the initial state $|00\rangle$, from which it is excited into the $|10\rangle$ or $|11\rangle$ states (see the blue sideband peak (dashed line) at 9.48 GHz for 13 dB more power). **b**, Coupled Rabi oscillations: the blue sideband is excited and the switching probability is recorded as a function of the pulse length for different microwave powers (plots are shifted vertically for clarity). For large microwave powers, the resonance peak of the blue sideband is shifted to 9.15 GHz. When detuning the microwave excitation away from resonance, the Rabi oscillations become faster (bottom four curves). These oscillations are suppressed by preparing the system in the $|10\rangle$ state with a π pulse and revived after a 2π pulse (top two curves in **b**). **c**, Coupled Rabi oscillations: after a π pulse on the qubit transition ($|00\rangle \rightarrow |10\rangle$) we excite the red sideband at 3.58 GHz. The switching probability shows coherent oscillations between the states $|10\rangle$ and $|01\rangle$, at various microwave powers (the curves are shifted vertically for clarity). The decay time of the coherent oscillations in **a** and **b** is ~ 3 ns.

the oscillator involved is indeed the SQUID plasma mode, we repeated the above measurements in the presence of an offset bias current I_{boff} which decreases the plasma frequency following¹⁹ $\nu_p(1 - (I_{\text{boff}}/I_c)^2)^{1/4}$, where I_c is the SQUID critical current (4.2 μ A). The data in Fig. 1c show the distance between the qubit peak for $F_L = 6.4$ GHz and the blue/red sidebands (down/up triangles) that decreases together with the oscillator resonance (circles).

To realize quantum operations on the qubit only, we apply a resonant microwave pulse with frequency $F_{\text{mw}} = F_L$. The operation is performed at the qubit symmetry point $\gamma_q = \pi$ where $F_L = \Delta$. In Fig. 2a, the SQUID switching probability is plotted against the microwave pulse length for three microwave power levels. The observed Rabi oscillations decay within ~ 30 ns. Remarkably, we can reach Rabi frequencies comparable to the Larmor frequency (up to 6.6 GHz). Using Fourier transformation, we extract the Rabi frequency as a function of the microwave amplitude (Fig. 2b). In the weak driving regime, the Rabi frequency increases linearly with the microwave power, as expected⁶. Near the oscillator resonance ν_p , we see two frequencies in the spectrum, a behaviour which is probably caused by the qubit–oscillator coupling. At even higher microwave powers, the spectrum exhibits again a second frequency component at Δ . A qualitatively similar behaviour is also obtained in numerical simulations (see Fig. 2c) when we consider the qubit driven by an additional term $(1/2)\hbar F_1 \cos(\Delta t)$ in H_q (F_1 and Δ are the microwave amplitude and frequency, respectively).

We now turn to the conditional dynamics resulting from the qubit–oscillator coupling. We first determine the blue and red sideband resonant frequencies by spectroscopic means using a two-pulse sequence (Fig. 3a). The qubit is prepared in the excited state by a π pulse at the Larmor frequency. A second pulse (18 ns) of variable frequency induces resonant qubit de-excitation (dips in Fig. 3a, top trace) marking the red sideband and the Larmor frequency. Similarly, after a 2π pulse which places the qubit in its ground state, we search for resonant excitations (peaks in Fig. 3a, bottom trace) that mark the Larmor frequency and the blue sideband. No resonance is seen on the red sideband, showing that the oscillator is in its ground state with a large probability. Note that in order to excite the blue sideband, we have to increase the microwave power by at least 10 dB, probably due to less effective microwave transmission in the 8–9 GHz range (note also the absence of spectroscopy peaks in this frequency range in Fig. 1b). At high microwave powers, we observe radiative shifts²⁰ of the resonances. We now exploit these resonances to study the dynamics of the

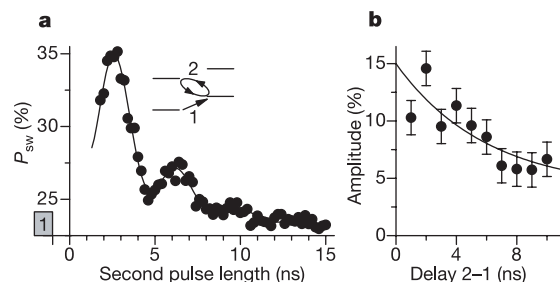


Figure 4 Oscillator relaxation time. **a**, Rabi oscillations between the $|01\rangle$ and $|10\rangle$ states (during pulse 2 in the inset) obtained after applying a first pulse (1) in resonance with the oscillator transition. Here, the interval between the two pulses is 1 ns. The continuous line represents a fit using an exponentially decaying sinusoidal oscillation plus the background (due to the relaxation into the ground state). The oscillation's decay time is $\tau_{\text{coh}} = 2.9$ ns, whereas the background decay time is ~ 4 ns. **b**, The amplitude of Rabi oscillations as a function of the interval between the two pulses (the vertical bars represent standard error bars estimated from the fitting procedure, see **a**). Owing to the oscillator relaxation, the amplitude decays in $\tau_{\text{rel}} \approx 6$ ns (the continuous line represents an exponential fit).

coupled system by applying pulses of varying length. In Fig. 3b, Rabi oscillations are shown for the $|00\rangle$ to $|11\rangle$ transition. When the microwave frequency is detuned from resonance, the Rabi oscillations are accelerated (bottom four curves, to be compared with the fifth curve). After a π pulse which prepares the system in the $|10\rangle$ state, these oscillations are suppressed (second curve in Fig. 3b). After a 2π pulse they are revived (first curve in Fig. 3b). In the case of Fig. 3c, the qubit is first excited onto the $|10\rangle$ state by a π pulse, and a second pulse in resonance with the red sideband transition drives the system between the $|10\rangle$ and $|01\rangle$ states. The Rabi frequency depends linearly on the microwave amplitude, with a smaller slope compared to the bare qubit driving. During the time evolution of the coupled Rabi oscillations shown in Fig. 3b and c, the qubit and the oscillator experience a time-dependent entanglement, although the present data do not permit us to quantify it to a sufficient degree of confidence.

The sideband Rabi oscillations of Fig. 3 show a short coherence time (~ 3 ns), which we attribute mostly to the oscillator relaxation. To determine its relaxation time, we performed the following experiment. First, we excite the oscillator with a resonant low power microwave pulse. After a variable delay Δt , during which the oscillator relaxes towards $n = 0$, we start recording Rabi oscillations on the red sideband transition (see Fig. 4a for $\Delta t = 1$ ns). The decay of the oscillation amplitude as a function of Δt corresponds to an oscillator relaxation time of ~ 6 ns (Fig. 4b), consistent with a quality factor of 100–150 estimated from the width of the ν_p resonance. The exponential fit (continuous line in Fig. 4b) shows an offset of $\sim 4\%$ due to thermal effects. To estimate the higher bound of the sample temperature, we consider that the visibility of the oscillations presented here (Figs 2–4) is set by the detection efficiency and not by the state preparation. When related to the maximum signal of the qubit Rabi oscillations of $\sim 40\%$, the 4%-offset corresponds to $\sim 10\%$ thermal occupation of oscillator excited states (an effective temperature of ~ 60 mK). Consistently, we also observe low-amplitude red sideband oscillations without preliminary microwave excitation of the oscillator.

We have demonstrated coherent dynamics of a coupled superconducting two-level plus harmonic oscillator system, implying that the two subsystems are entangled. Increasing the coupling strength and the oscillator relaxation time should allow us to quantify the entanglement, as well as to study non-classical states of the oscillator. Our results provide strong indications that solid-state quantum devices could in future be used as elements for the manipulation of quantum information. \square

Received 25 May; accepted 5 July 2004; doi:10.1038/nature02831.

1. Nielsen, M. A. & Chuang, I. L. *Quantum Computation and Quantum Information* (Cambridge Univ. Press, Cambridge, 2000).
2. Nakamura, Y. *et al.* Coherent control of macroscopic quantum states in a single-Cooper-pair box. *Nature* **398**, 786–788 (1999).
3. Vion, D. *et al.* Manipulating the quantum state of an electrical circuit. *Science* **296**, 886–889 (2002).
4. Yu, Y., Han, S., Chu, X., Chu, S. & Wang, Z. Coherent temporal oscillations of macroscopic quantum states in a Josephson junction. *Science* **296**, 889–892 (2002).
5. Martinis, J. M., Nam, S., Aumentado, J. & Urbina, C. Rabi oscillations in a large Josephson-junction qubit. *Phys. Rev. Lett.* **89**, 117901 (2002).
6. Chiorescu, I., Nakamura, Y., Harmans, C. J. P. M. & Mooij, J. E. Coherent quantum dynamics of a superconducting flux qubit. *Science* **299**, 1869–1871 (2003).
7. Pashkin, Yu. A. *et al.* Quantum oscillations in two coupled charge qubits. *Nature* **421**, 823–826 (2003).
8. Berkley, A. J. *et al.* Entangled macroscopic quantum states in two superconducting qubits. *Science* **300**, 1548–1550 (2003).
9. Majer, J. B., Pavauw, F. G., ter Haar, A. C. J., Harmans, C. J. P. M. & Mooij, J. E. Spectroscopy on two coupled flux qubits. Preprint at (<http://arxiv.org/abs/cond-mat/0308192>) (2003).
10. Izmalkov, A. *et al.* Experimental evidence for entangled states formation in a system of two coupled flux qubits. Preprint at (<http://arxiv.org/abs/cond-mat/0312332>) (2003).
11. Yamamoto, T., Pashkin, Yu. A., Astafiev, O., Nakamura, Y. & Tsai, J. S. Demonstration of conditional gate operation using superconducting charge qubits. *Nature* **425**, 941–944 (2003).
12. Leibfried, D., Blatt, R., Monroe, C. & Wineland, D. Quantum dynamics of single trapped ions. *Rev. Mod. Phys.* **75**, 281–324 (2003).
13. Mandel, O. *et al.* Controlled collisions for multi-particle entanglement of optically trapped atoms. *Nature* **425**, 937–940 (2003).
14. Raimond, J. M., Brune, M. & Haroche, S. Manipulating quantum entanglement with atoms and photons in a cavity. *Rev. Mod. Phys.* **73**, 565–582 (2001).

15. Mooij, J. E. *et al.* Josephson persistent-current qubit. *Science* **285**, 1036–1039 (1999).
16. van der Wal, C. H. *et al.* Quantum superposition of macroscopic persistent-current states. *Science* **290**, 773–777 (2000).
17. Burkard, G. *et al.* Asymmetry and decoherence in double-layer persistent-current qubit. Preprint at (<http://arxiv.org/abs/cond-mat/0405273>) (2004).
18. Goorden, M. C., Thorwart, M. & Grifoni, M. Entanglement spectroscopy of a driven solid-state qubit and its detector. Preprint at (<http://arxiv.org/abs/cond-mat/0405220>) (2004).
19. Tinkham, M. *Introduction to Superconductivity* 2nd edn (McGraw-Hill, New York, 1996).
20. Cohen-Tannoudji, C., Dupont-Roc, J. & Grynberg, G. *Atom-photon Interactions: Basic Processes and Applications* Ch. II E (Wiley & Sons, New York, 1992).

Acknowledgements We thank A. Blais, G. Burkard, D. DiVincenzo, G. Falci, M. Grifoni, S. Lloyd, S. Miyashita, T. Orlando, R. N. Schouten, L. Vandersypen and F. K. Wilhelm for discussions. This work was supported by the Dutch Foundation for Fundamental Research on Matter (FOM), the EU Marie Curie and SQUBIT grants, and the US Army Research Office.

Competing interests statement The authors declare that they have no competing financial interests.

Correspondence and requests for materials should be addressed to I.C. (chiorescu@pa.msu.edu) and J.E.M. (mooij@qt.tn.tudelft.nl).

Strong coupling of a single photon to a superconducting qubit using circuit quantum electrodynamics

A. Wallraff¹, D. I. Schuster¹, A. Blais¹, L. Frunzio¹, R.-S. Huang^{1,2}, J. Majer¹, S. Kumar¹, S. M. Girvin¹ & R. J. Schoelkopf¹

¹Departments of Applied Physics and Physics, Yale University, New Haven, Connecticut 06520, USA

²Department of Physics, Indiana University, Bloomington, Indiana 47405, USA

The interaction of matter and light is one of the fundamental processes occurring in nature, and its most elementary form is realized when a single atom interacts with a single photon. Reaching this regime has been a major focus of research in atomic physics and quantum optics¹ for several decades and has generated the field of cavity quantum electrodynamics^{2,3}. Here we perform an experiment in which a superconducting two-level system, playing the role of an artificial atom, is coupled to an on-chip cavity consisting of a superconducting transmission line resonator. We show that the strong coupling regime can be attained in a solid-state system, and we experimentally observe the coherent interaction of a superconducting two-level system with a single microwave photon. The concept of circuit quantum electrodynamics opens many new possibilities for studying the strong interaction of light and matter. This system can also be exploited for quantum information processing and quantum communication and may lead to new approaches for single photon generation and detection.

In atomic cavity quantum electrodynamics (QED), an isolated atom with electric dipole moment d interacts with the vacuum state electric field E_0 of a cavity. The quantum nature of the field gives rise to coherent oscillations of a single excitation between the atom and the cavity at the vacuum Rabi frequency $\nu_{\text{Rabi}} = 2dE_0/\hbar$, which can be observed when ν_{Rabi} exceeds the rates of relaxation and decoherence of both the atom and the field. This effect has been observed in the time domain using Rydberg atoms in three-dimensional microwave cavities³ and spectroscopically using alkali atoms in very small optical cavities with large vacuum fields⁴.

Coherent quantum effects have been recently observed in several superconducting circuits^{5–10}, making these systems well suited for use as quantum bits (qubits) for quantum information processing.